In situ fabrication of bismuth oxyiodide ($Bi_7O_9I_3$/Bi_5O_7I) n-n heterojunction for enhanced degradation of triclosan (TCS) under simulated solar light irradiation

Chun Chang[a,*], Huanchun Yang[a], Weina Mu[a], Yanrong Cai[a], Lixia Wang[a], Liping Yang[b], Hongwei Qin[a]

[a] Department of Environmental Science and Engineering in College of Chemistry and Chemical Engineering, Bohai University, Jinzhou 121013, PR China
[b] College of Environmental Science and Engineering, Nankai University, Tianjin 300350, PR China

ABSTRACT

Triclosan (TCS) is considered a potential pollutant and it threatens human health and survival of other organisms. $Bi_7O_9I_3$ was successfully synthesized with a simple solvothermal method. In this study, a novel n-n heterojunction photocatalyst ($Bi_7O_9I_3$/Bi_5O_7I) was formed by in situ calcination of $Bi_7O_9I_3$. It was obvious that the morphology had changed in the calcination process from the original sheet structure to the bone-stick-like structure, but still maintained a spherical 3-dimensional structure. At the same time, two kinds of lattice fringes were identified from the HR-TEM in sample $Bi_7O_9I_3$-450 which effectively proved the formation of the $Bi_7O_9I_3$/Bi_5O_7I heterojunction. This composite photocatalyst could effectively remove TCS from the water. Its photocatalytic efficiency was significantly improved compared with the pure $Bi_7O_9I_3$. This was attributed to the internal electric field in the composite catalyst which facilitated the transport and migration of photo-generated carriers. The degradation mechanism of TCS was analyzed, and the electron reduction and $\cdot O_2{}^-$ species and singlet oxygen oxidation played essential role in the TCS degradation by radical scavenger experiment. These species could react with TCS pollutants, leading to the degradation of TCS. Finally, the eleven degradation products were identified by the HPLC-MS method, and the two major reaction pathways were deduced.

1. Introduction

Nowadays, with the development of industry, the environmental pollution is getting worse. Massive of personal care products (PCPs) have the potential threat to animals, plants and human. Triclosan (TCS) was considered a broad-spectrum bacteriostatic germicide which had been used in a wide range of PCPs [1,2], such as toothpaste, shampoo, skin-care lotion, and even in children-toys [3]. TCS and some of its derivatives had been detected in wastewaters [4], surface water and soil [5], and even in biological samples, such as fish and the human body [6,7]. TCS has a relatively high octanol-water partition coefficient, leading to its bio-concentration in biota and bio-magnification via food chain, ultimately threatening the safety of organisms. The major treatment methods for TCS include biological, physical and chemical processes. The conventional biological treatment processes often can't efficiently degrade TCS in sewage treatment plants [8]. It is the main reason that the TCS biodegradation needs a long cycle, and high

concentrations of TCS will inhibit the growth of microorganism [9]. In addition, the adsorption on porous adsorbents as the physical method is regarded as an effective way to reduce TCS [8]. However, the adsorption capacity of adsorbents is limited, and the adsorbed TCS might be desorbed and cause secondary pollution. Therefore, it is imperative that an efficient and convenient method for TCS degradation is developed. Recently, semiconductor photocatalysis has attracted great interest and widespread attention due to its effective activity and low toxicity.

Bismuth oxyhalides (BiOCl, BiOBr and BiOI) have been reported to be an outstanding family of promising photocatalyst due to their open and layered tetragonal crystal structure and suitable band gaps [10–12]. Among them, bismuth oxyiodide ($Bi_xO_yI_z$) is an outstanding visible-light driven semiconductor photocatalyst, resulting from unique layered structure with special internal eletrostatic field and a narrow band gap [13]. Except for BiOI, other bismuth oxyiodides have been reported in some correlative literatures. For example, the ball flower-like mesoporous $(BiOBr)_x(Bi_7O_9I_3)_{1-x}$ was synthesized by the facile one-

pot ultrasound-assisted solvothermal method and applied to degradation of levofloxacin (LVFX) under simulated solar light [14]. And Liang et.al designed layered 2D/2D Bi@Bi$_5$O$_7$I/rGO heterojunction composite through a facile charge mediated self-assembly strategy for degradation of LVFX under visible light irradiation [15]. Furthermore, N-doped carbon quantum dots modified Bi$_4$O$_5$I$_2$ hollow nanotubes composite photocatalyst was fabricated successfully and exhibited excellent broad spectrum photocatalytic performance for bisphenol A (BPA) removal [16]. At present, the construction of heterojunction structure to improve the photocatalytic efficiency has made great progress. It is well known that p-n heterojunctions can be formed at the boundary between p type and n type semiconductors, and heterojunction structure is an efficacious architecture for separation of photo-generated electron-hole pairs [17]. Recently, it is reported that p-p and n-n heterojunctions via combining two appropriate semiconductors can also speed up the interfacial charges transferring rate to adsorbed substances due to the formation of inner electric fields [18–20]. However, there were few reports about the research on n-n type heterojunction of bismuth oxyiodides [21]. In addition, an in situ fabrication method, which has been proven to be effective synthesis strategy, is always used to construct heterojunction catalyst for establishing firm interface interaction. Nevertheless, a number of previous reported works about the synthesis of heterojunction structure mainly involve depositing or mechanical-compositing one material on the surface of catalyst [22]. It is known all that the complex and time-consuming synthesis procedures of in situ fabrication may result in low production yield and high cost [23]. Thus, it is highly desirable to develop an in situ calcination route to prepare heterojunction photocatalysts for producing more firm and intimate interfacial interaction. It may effectively improve catalytic performance of photocatalyst due to the fast separation and transfer of photo-generated electron-hole pairs.

In this study, we successfully developed a novel n-n heterojunction structure photocatalyst (Bi$_7$O$_9$I$_3$/Bi$_5$O$_7$I) via the facile and cost-effective method. And the photocatalytic activities were evaluated by the degradation of TCS aqueous solution under simulated solar irradiation. According to the trapping experiments, the possible decomposition mechanism of TCS by Bi$_7$O$_9$I$_3$/Bi$_5$O$_7$I was analyzed to better understand the underlying phenomenon in the photocatalytic process. Moreover, the degradation products of TCS were detected by high performance liquid phase coupled with mass spectrometer (HPLC-MS). The degradation reaction pathways of TCS were elaborated in detail based on the detection of the products. This paper provides a feasible method to synthesis n-n heterojunction structure photocatalyst for removal of TCS.

2. Experimental sections

2.1. Preparation and characterization of photocatalysts

The Bi$_7$O$_9$I$_3$ was synthesized as reported previously with a few modifications [24]. The detailed procedure was given in Supporting Information and Scheme 1. The final sample of Bi$_7$O$_9$I$_3$ was calcinated at 350, 450, 550, 650, and 750 ℃ in the muffle furnace, respectively. The products were denoted as Bi$_7$O$_9$I$_3$-350, Bi$_7$O$_9$I$_3$-450, Bi$_7$O$_9$I$_3$-550, Bi$_7$O$_9$I$_3$-650, and Bi$_7$O$_9$I$_3$-750. The prepared samples were characterized by means of XRD, TG, SEM, HR-TEM, XPS, UV–vis DRS, FT-IR, Raman, ESR, and Mott-Schottky plots. The detailed information about the characterization methods was described in Supporting Information.

2.2. Photoelectrochemical measurement

In this article, the photoelectrochemical measurements were carried out using a CHI614E electrochemical analyzer. The samples were characterized in a standard three-electrode setup with a quartz window to facilitate illumination in a 0.5 mol/L Na$_2$SO$_4$ aqueous solution. The photocatalyst/ITO electrode was used as the working electrode with an illumination area of 1 cm^2. A platinum foil and a saturated calomel

electrode (SCE) were used as the counter and reference electrode, respectively. The light source was provided with a solar simulator (Newport, AM 1.5, 100 mW/cm^2). Electrochemical impedance spectra (EIS) were conducted at similar conditions as described above for the photoelectrochemical test. A sinusoidal ac perturbation of 5 mV was applied to the electrode over the frequency range of 0.01-10^5 HZ.

2.3. Photocatalytic degradation experiments

The activity of photocatalyst was reflected by the degradation of TCS in aqueous solution under simulated solar irradiation. Batch experiments were conducted in a BL-GHX photochemical reactor using 500 W xenon lamp as light resource. The light intensity of the xenon lamp was 10 × 1000 uw/cm^2. The area for light irradiation was calculated at approximately 33.75 cm^2 for each quartz tube. 0.05 g photocatalyst powder was dispersed into the 50 mL of TCS (20 mg/L) in a quartz tube. Before the irradiation, the whole reaction system was magnetically stirred in the darkness for 30 min to ensure the adsorption-desorption equilibrium. A certain amount of suspension was taken out at preset time intervals and centrifuged under 5000 rpm before the analysis. The concentration of the supernatant was measured by UV–vis spectrophotometer at the maximum absorption wavelength of 280 nm. Then the removal efficiency of TCS was calculated as η (%) = (1-C$_t$/C$_0$) ×100, where C$_0$ (mg/L) and C$_t$ (mg/L) are the initial and reaction concentrations of TCS. The detail information about recycling tests was showed in Supporting Information.
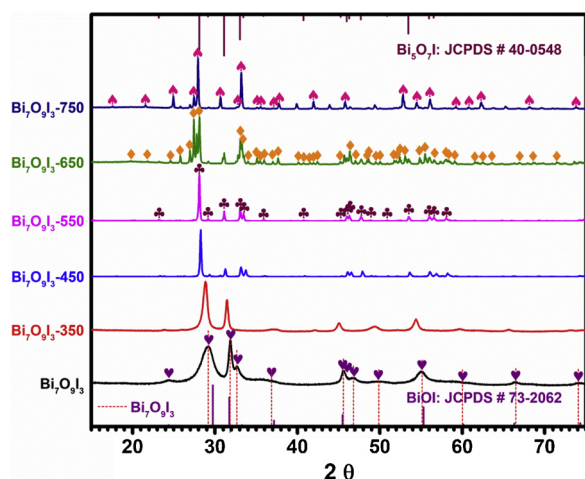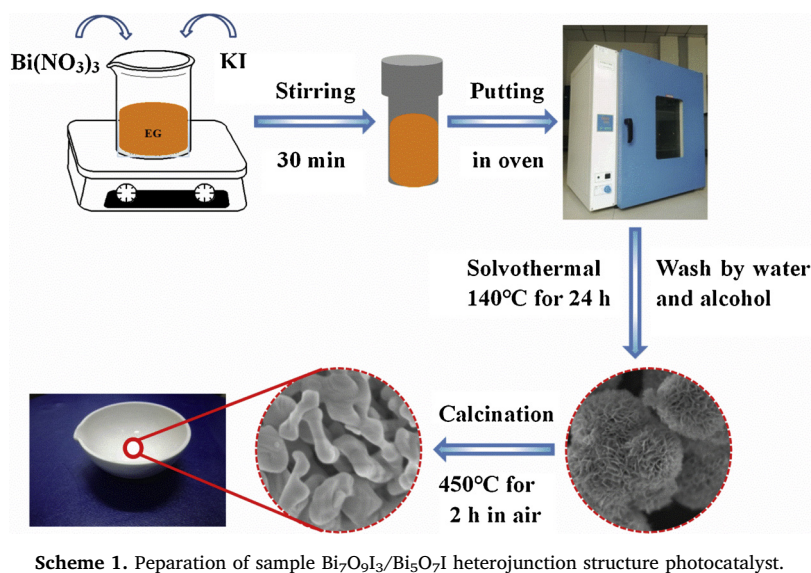
2.4. Identification of the TCS degradation products

Degradation products of TCS were analyzed through employing a high performance liquid chromatography and mass spectrometer (HPLC-MS, Waters Xevo TQS, USA). The HPLC-MS analysis was conducted with Waters BEH C18 (2.1 × 1.7 × 50 mm) column. The mobile phases were composed of 0.3% formic acid in water (A) and methanol (B), a flow rate of 0.3 mL/min. The seal wash period was 5 min. The mass spectra (*m/z* 58–1000) were operated in negative ion mode by using an electrospray ion (ESI) source, and the desolvation gas flow was 800 L/Hr.

3. Result and discussion

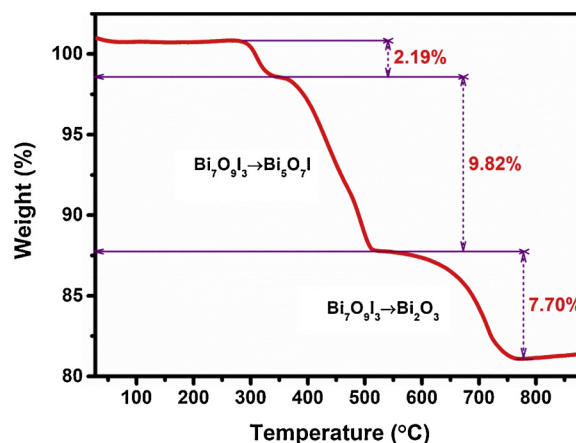### 3.1. Characterization of the photocatalysts

X-ray diffraction (XRD) analysis was carried out to identify the crystal structure of the samples. As shown in Fig.1, the diffraction peaks of the catalysts prepared at 140 ℃ for 24 h was quite similar to the diffraction peaks of BiOI [JCPDS No. 73-2062] in the full-range (2θ = 10-80°), but the positions of some diffraction peaks shifted slightly to smaller diffraction angles. It could be understood that the addition of extra bismuth and oxygen atoms existed in the original BiOI structure system, causing the lattice expansion and distortion of the crystal structure. Then all the characteristic diffraction peaks of the as-synthesized sample could match well with those of Bi$_7$O$_9$I$_3$ at 28.7, 31.5, 36.8, 45.2, 49.2, and 54.6° [25]. In addition, no other apparent diffraction peaks were observed in the diffractive patterns, indicating that pure Bi$_7$O$_9$I$_3$ crystal phase was obtained. As the temperature increased to 350 ℃, the diffraction peaks slightly shifted left relative to peaks of Bi$_7$O$_9$I$_3$. With the continuous increasing of the temperature, another phase appeared, and the diffraction peaks of Bi$_7$O$_9$I$_3$-550 were consisted with the standard card of Bi$_5$O$_7$I [JCPDS No. 40-0548]. No peaks of other impurities were observed in this sample, suggesting the formation of pure Bi$_5$O$_7$I. Besides, it could be found that all diffraction peaks of Bi$_7$O$_9$I$_3$-450 were in good agreement with diffraction peaks of Bi$_7$O$_9$I$_3$ and Bi$_5$O$_7$I. Based on the XRD diffraction peaks of Bi$_7$O$_9$I$_3$-350 and the analysis results of other samples (Bi$_7$O$_9$I$_3$-450, Bi$_7$O$_9$I$_3$-550), it was speculated that Bi$_7$O$_9$I$_3$-350 might be also composed of Bi$_7$O$_9$I$_3$ and

Scheme 1. Peparation of sample $Bi_7O_9I_3/Bi_5O_7I$ heterojunction structure photocatalyst.

Fig. 1. X-ray diffraction (XRD) patterns of $Bi_7O_9I_3$, $Bi_7O_9I_3$-350, $Bi_7O_9I_3$-450, $Bi_7O_9I_3$-550, $Bi_7O_9I_3$-650 and $Bi_7O_9I_3$-750. ♥: $Bi_7O_9I_3$, ♣: Bi_5O_7I, ◆:α-Bi_2O_3, ♠ :ω-Bi_2O_3.

Fig. 2. TG profile of $Bi_7O_9I_3$ sample in air flow.

Bi_5O_7I, but the percent of Bi_5O_7I in $Bi_7O_9I_3$-350 was less than $Bi_7O_9I_3$-450. When the temperature increased to 650 °C, the characteristic peaks of $Bi_7O_9I_3$ disappeared. The $Bi_7O_9I_3$-650 could be indexed into the monoclinic phase of α-Bi_2O_3 [JCPDS No. 41-1449] and Bi_5O_7I. However, when the temperature finally reached 750 °C, and the characteristic peaks of $Bi_7O_9I_3$-750 could be assigned to monoclinic phases of Bi_2O_3 (α-Bi_2O_3) and triclinic phases of Bi_2O_3 (ω-Bi_2O_3) [JCPDS No. 50-1088] [26].

In order to further confirm the composition of sample, the thermogravimetric (TG) of the $Bi_7O_9I_3$ was analyzed. As a matter of fact, all the obvious weight losses were owing to step-by-step iodine escape during the heating process. The thermolysis of $Bi_7O_9I_3$ was mainly characterized by two mass loss steps, and the result was demonstrated by Fig.2. The initial weight loss (2.06%) might be caused by mixing some BiOI in the synthesized $Bi_7O_9I_3$. In the temperature range of 340–500 °C, the weight loss (about 9.82%) might be ascribed to the transformation from $Bi_7O_9I_3$ to Bi_5O_7I which was coincided with stoichiometric proportion (9.57%) of this conversion between $Bi_7O_9I_3$ and Bi_5O_7I. However, when the temperature increased more than 600 °C, Bi_5O_7I was beginning to transform until the temperature reached 770 °C. In this temperature interval, the weight loss of sample was 7.70%, which suggested that the sample hardly released all I element from Bi_5O_7I to Bi_2O_3 [22]. Moreover, this phenomenon indicated that Bi_5O_7I

could stably exist between 500 and 600℃. Finally, the bismuth oxyiodide was transformed to the bismuth oxide. The result of the TG analysis was in agreement with the XRD.

To investigate the morphologies and the structures of samples, scanning electron microscopy (SEM) images of samples $Bi_7O_9I_3$, $Bi_7O_9I_3$-350, $Bi_7O_9I_3$-450, $Bi_7O_9I_3$-550, $Bi_7O_9I_3$-650, and $Bi_7O_9I_3$-750 were shown in Fig. 3 and Fig S1. From the typical SEM image of $Bi_7O_9I_3$, we could observe that pure $Bi_7O_9I_3$ sample exhibited a similar flower-like hierarchical spherical structure in the Fig. 3 (a) and Fig. S1 (a). However, with the increase of the calcination temperature, the morphologies of the samples were changed as displayed by SEM images. When the temperature reached 350 °C, the layered structure of $Bi_7O_9I_3$ obviously became thick. At the same time, the flower structure was also not complete and there had some small holes on the surface. As shown in Fig. 3 (c) and Fig. S1 (c), the morphologies of sample transformed into bone-stick-like and still maintained a spherical structure when the temperature reached 450 °C. The spherical structure disappeared and exhibited the bulk-like structure at 550 °C, there was no other impurities on the smooth sample surface [27]. However, some small bulk particles were clearly deposited on the surface of the $Bi_7O_9I_3$-550 when the calcination temperature reached 650 °C. Based on XRD analysis, this might be because the monoclinic Bi_2O_3 particles were attached to the surface of Bi_5O_7I. Until it reached the temperature of 750 °C, the blocky-like were formed as shown in Fig. 3 (f) and Fig. S1 (f) [24]. Moreover, the microstructure of the $Bi_7O_9I_3$-450 photocatalyst was examined by field emission transmission electron microscopy (FE-

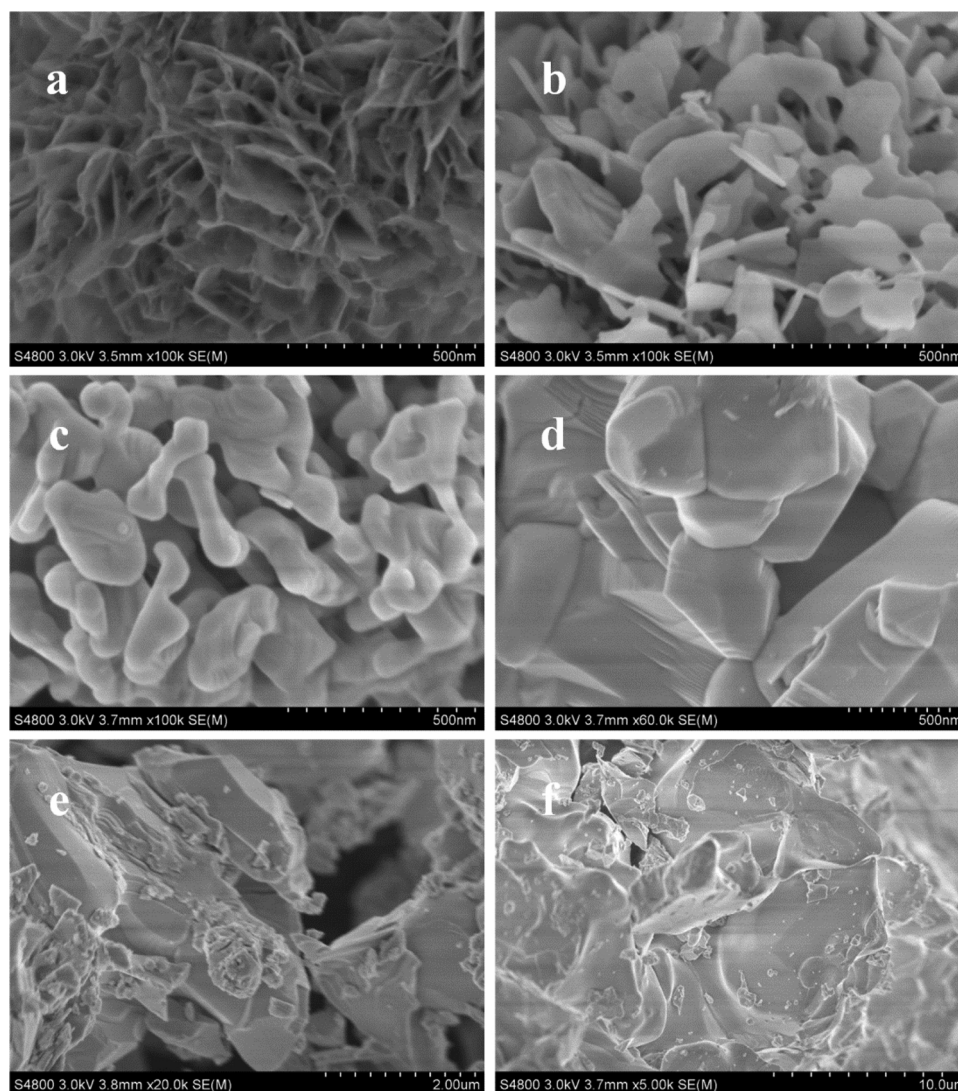**Fig. 3.** SEM images of $Bi_7O_9I_3$ (a), $Bi_7O_9I_3$-350 (b), $Bi_7O_9I_3$-450 (c), $Bi_7O_9I_3$-550 (d), $Bi_7O_9I_3$-650 (e), $Bi_7O_9I_3$-750 (f).

TEM), and shown in Fig. 4. As shown in Fig. 4 (a), the diameter of $Bi_7O_9I_3$-450 spherical bone-stick-like was about 3.0 μm, and aspect ratio of bone-stick-like was approximately 200:100 nm from Fig. 4 (b). A HR-TEM image in Fig. 4 (c) showed two kinds of lattice fringes, the phase with the lattice fringes (3.06 Å) could be observed which indexed to the plane (012) of $Bi_7O_9I_3$ [28]. On the other hand, there revealed the other one lattice spacing of 2.88 Å, which corresponded to the (004) plane of Bi_5O_7I [29,30]. The selected area electron diffraction (SAED) was demonstrated on the Fig. 4 (d). It clearly revealed that the angle of (012) and (004) were 72.0° between $Bi_7O_9I_3$ and Bi_5O_7I which was in keeping with the theoretical angle that of 70.5° for (012) and (004). Based on the above analysis, the result suggested that the heterogeneous structure of $Bi_7O_9I_3$ and Bi_5O_7I was formed. It was consistent with the XRD and TG measurement of $Bi_7O_9I_3$-450, which could effectively promote the separation and transmission of photo-generated charge carries, further increasing the catalytic activity of the photocatalyst.

The chemical composition and the valence state of the $Bi_7O_9I_3$ and $Bi_7O_9I_3$-450 were analyzed by the X-ray photoelectron spectroscopy (XPS). Fig. 5 (a)–(c) were characteristic peaks of the inner electron binding energy of O 1s, Bi 4f, and I 3d, respectively. As the Fig. 5 (a) shown, the spectra of O1s for $Bi_7O_9I_3$ were fitted with three peaks which could be found at 529.25, 530.08, 530.92 eV, respectively. The peaks at 529.25, 530.08 eV could be assigned to the Bi-O bonds and I-O

bonds [31,32]. And the peak located at 530.92 eV indicated that some the other components (H_2O, OH, O_2) absorbed on the surface of catalyst [33]. The Bi 4f could be presented in the Fig. 5 (b), the Bi $4f_{5/2}$ and Bi $4f_{7/2}$ binding energy peaks for $Bi_7O_9I_3$ were focused on 158.45 and 163.70 eV. The splitting energy between Bi $4f_{5/2}$ and Bi $4f_{7/2}$ were 5.25 eV for $Bi_7O_9I_3$, which suggested that the valence state of Bi^{3+} in $Bi_7O_9I_3$ [34]. The binding energy of I 3d could be seen in Fig. 5 (c), the I 3d spectra included the peaks at 618.15 eV (I $3d_{3/2}$) and 629.65 eV (I $3d_{5/2}$), respectively, suggesting the valence state of I^{-1} in $Bi_7O_9I_3$ [12]. A positive shift in the Bi 4f and I 3d binding energies were observed when $Bi_7O_9I_3$ was calcined at 450 ℃. It was speculated that the chemical interactions might exist between $Bi_7O_9I_3$ and Bi_5O_7I rather than simple mechanical mixing. This result could fully explain the heterojunction formation of $Bi_7O_9I_3$-450 composites which might promote transfer and separation of the electron and hole pairs. So the photocatalytic efficiency could be improved during the TCS degradation [34].

The Fourier transform infrared spectroscopy (FT-IR) spectra of all samples were shown in Fig. 6. In the FT-IR spectra of $Bi_7O_9I_3$, $Bi_7O_9I_3$-350 and $Bi_7O_9I_3$-450, there was a broad absorption bond at 3441 cm^{-1} in the Fig. 6 (a), corresponding to the stretching vibration absorption of ν (O−H) groups from the free water molecules, and the peak at 1647 cm^{-1} was assigned to the δ (O−H) bending vibration absorption of free water molecules [18,35]. In the spectrum of $Bi_7O_9I_3$, a peak observed around 759 cm^{-1} was attributed to the asymmetrical
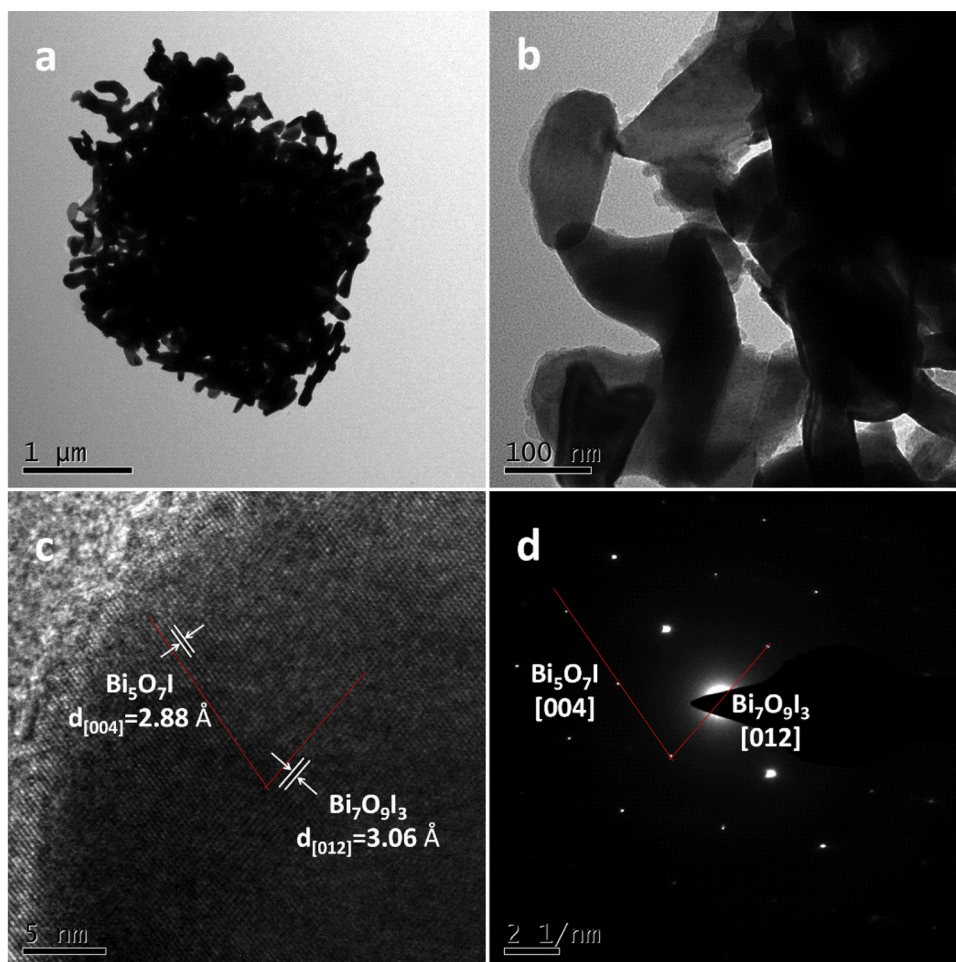
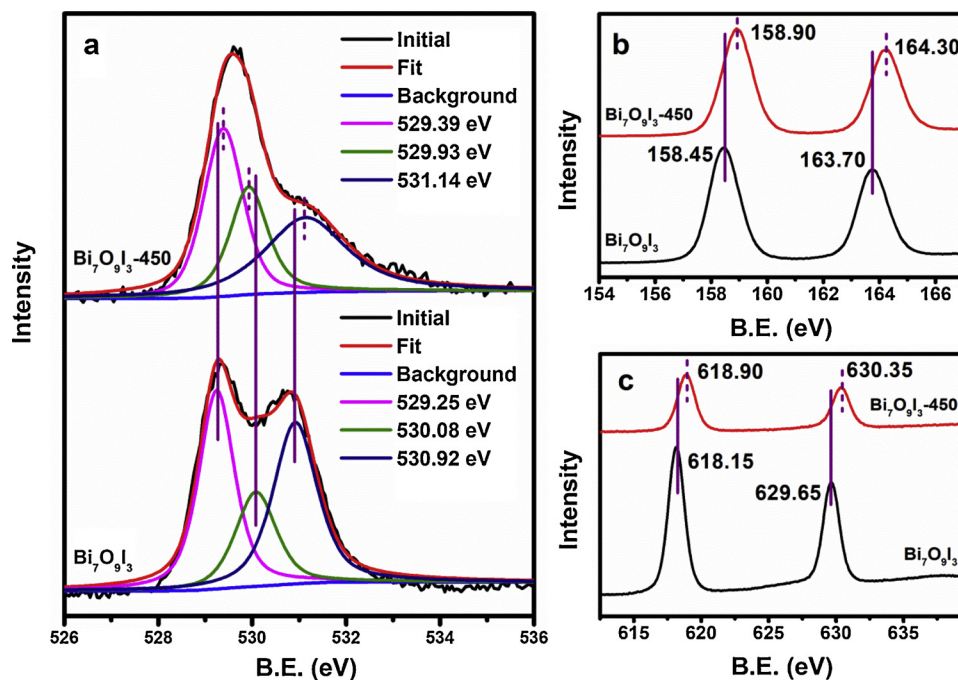**Fig. 4.** TEM images (a), (b); HRTEM image (c); selected area electron diffraction (SAED) (d) of $Bi_7O_9I_3$-450.

Fig. 5. XPS survey spectrum of $Bi_7O_9I_3$, $Bi_7O_9I_3$-450 and the corresponding high-resolution XPS spectra of O 1s (a), Bi 4f (b), and I 3d (c).
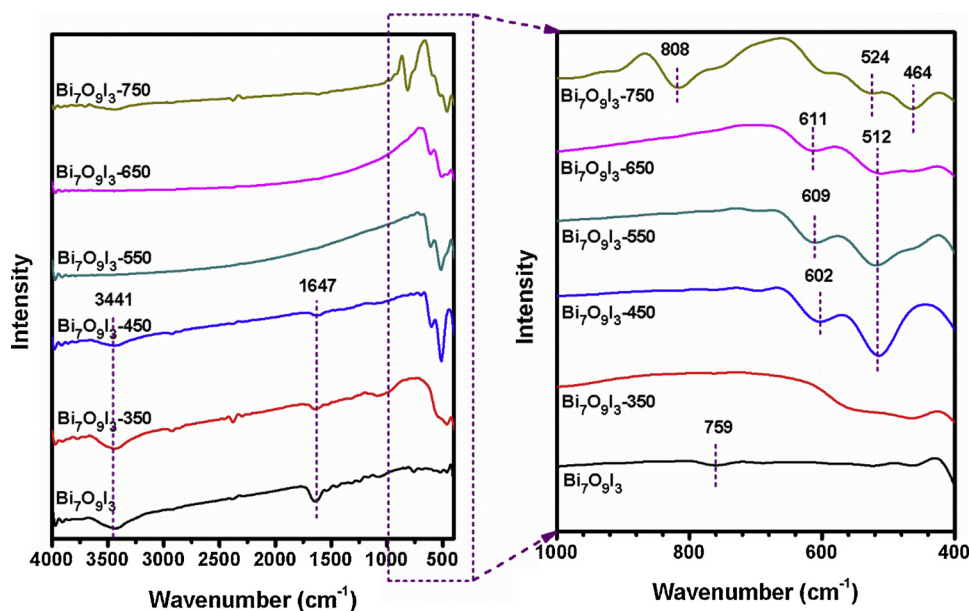
Fig. 6. FT-IR spectra of the $Bi_7O_9I_3$ and the samples at different calcination temperatures.

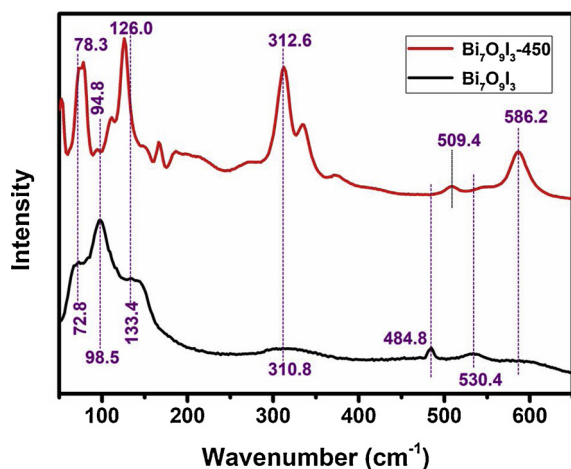**Fig. 7.** Raman spectra of $Bi_7O_9I_3$ and $Bi_7O_9I_3$-450.

stretching vibration of the Bi-–O bond [35]. For the samples of $Bi_7O_9I_3$-450 ($Bi_7O_9I_3/Bi_5O_7I$), $Bi_7O_9I_3$-550 (Bi_5O_7I), $Bi_7O_9I_3$-650 (Bi_5O_7I/α-Bi_2O_3), the absorption peaks at $512\,cm^{-1}$ were ascribed to the symmetrical A_{2u}-type vibrations of the Bi-–O bond [24,36]. However, for

the sample of $Bi_7O_9I_3$-750 (α-Bi_2O_3/ω- Bi_2O_3), the peaks slightly shifted to higher frequency region. And there were two new absorption peaks appearing at around $464\,cm^{-1}$ and $808\,cm^{-1}$, ascribing to the stretching vibration of Bi-–O bond and the asymmetrical stretching vibration of the Bi-–O bond [37]. In order to further illustrate the structure of the samples $Bi_7O_9I_3$ and $Bi_7O_9I_3$-450, Raman spectra were shown in Fig. 7. The three absorption peaks at 72.8, 98.5 and $133.4\,cm^{-1}$ were discovered for the sample $Bi_7O_9I_3$ which could be assigned to A_{1g} and E_g of the Bi-I stretching mode, respectively [38]. But for the sample of $Bi_7O_9I_3$-450, the intensity of each peak were changed obviously, which resulted from the heterojunction construction between $Bi_7O_9I_3$ and Bi_5O_7I, leading to the enlargement in bond energy [13]. Furthermore, the new peaks at 300-$600\,cm^{-1}$ for $Bi_7O_9I_3$-450 might be attributed to the change of Bi-O environment [39].

The UV–vis diffuse reflectance spectra (DRS) of the samples were emerged in the Fig. S2. The absorption wavelength edges of $Bi_7O_9I_3$, $Bi_7O_9I_3$-350, $Bi_7O_9I_3$-450, $Bi_7O_9I_3$-550, $Bi_7O_9I_3$-650, $Bi_7O_9I_3$-750 were located at 610, 520, 400, 480, 570, 580 nm, respectively. With the increase of temperature, the absorption edges of samples shifted blue in the range of 200~800 nm as compared to pure $Bi_7O_9I_3$ when the temperature was below 450 ℃, and the absorption edges of samples gradually shifted red more than 450 ℃ while the absorption intensity in the UV–vis light region became weak.

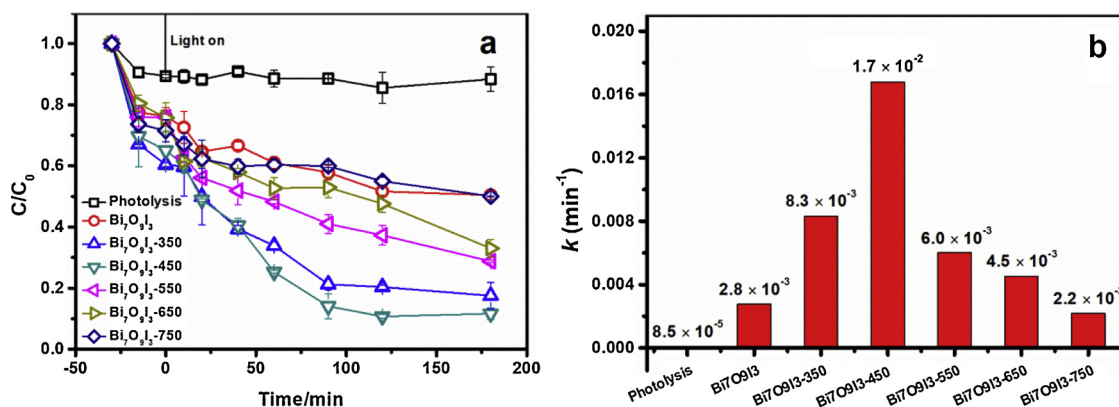**Fig. 8.** Photocatalytic degradation (a) and pseudo first-order rate constant (b) of TCS by $Bi_7O_9I_3$, $Bi_7O_9I_3$-350, $Bi_7O_9I_3$-450, $Bi_7O_9I_3$-550, $Bi_7O_9I_3$-650, and $Bi_7O_9I_3$-750 under simulated solar irradiation.

3.2. Photocatalytic activities

The photocatalytic activities of samples were evaluated by the degradation of TCS aqueous solution under simulated solar irradiation. As seen in Fig. 8 (a), TCS was hardly degraded in the absence of photocatalyst. However, TCS degradation could be observed in the presence of $Bi_7O_9I_3$, $Bi_7O_9I_3$-350, $Bi_7O_9I_3$-450, $Bi_7O_9I_3$-550, $Bi_7O_9I_3$-650, $Bi_7O_9I_3$-750, their removal efficiency were 49.60, 82.49, 89.28, 71.23, 66.99, and 49.93% after irradiation for 180 min, respectively. It was apparent that the photocatalytic performances of the samples treated by high temperature were higher than the pure $Bi_7O_9I_3$ for TCS degradation except the $Bi_7O_9I_3$-750 under simulated solar light irradiation. Meanwhile, the $Bi_7O_9I_3$-450 exhibited the highest photocatalytic activity than others. And the removal efficiency of $Bi_7O_9I_3$-450 ($Bi_7O_9I_3/Bi_5O_7I$) was almost twice that of pure $Bi_7O_9I_3$. The result was attributed to the formation of n-n heterojunction $Bi_7O_9I_3/Bi_5O_7I$ composite, which could improve the separation efficiency of photo-generated carriers and enhance the transfer of holes and electrons in the interfacial domain, thus $Bi_7O_9I_3$-450 exhibit more excellent photocatalytic activity.

In addition, the following pseudo first-order reaction kinetic model was used to have a better understand of the reaction kinetics for TCS degradation [17,40]:
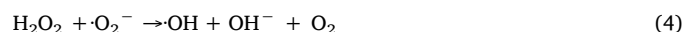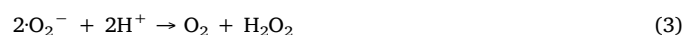
$$-\ln(C_t/C_0) = k\,t \tag{1}$$

where C_t (mg/L) is the concentration of TCS in aqueous phase at time t, the C_0 (mg/L) is the initial TCS concentration, and t (min) is the reaction time. Fig. 8 (b) showed the pseudo-first-order kinetics data for the photocatalytic degradation of TCS by different photocatalysts. The corresponding degradation rate constants (k) were 0.0028, 0.0083, 0.0168, 0.0060, 0.0045, and 0.0022 min^{-1} for the samples of $Bi_7O_9I_3$, $Bi_7O_9I_3$-350, $Bi_7O_9I_3$-450, $Bi_7O_9I_3$-550, $Bi_7O_9I_3$-650, and $Bi_7O_9I_3$-750, respectively. Apparently, the $Bi_7O_9I_3$-450 ($Bi_7O_9I_3/Bi_5O_7I$) exhibited the highest k value (0.0168 min^{-1}), which was about 6 times higher than that of pure $Bi_7O_9I_3$ (0.0028 min^{-1}). All these results illustrated that the n-n heterojunction $Bi_7O_9I_3/Bi_5O_7I$ composite could improve the photocatalytic performance of $Bi_7O_9I_3$ efficiently under simulated solar light irradiation [41].

The photoelectrochemical performance could be carried out by photocurrent response and electrochemical impedance spectroscopy (EIS) under simulated solar irradiation. As shown in Fig. 9 (a), it was clear that the photo-current density dropped significantly in the dark. However, the photo-current densities of the two photocatalysts increased in different level under simulated solar light irradiation. The photocurrent intensity generated by $Bi_7O_9I_3$-450 electrode was approximately quadruple of that induced by $Bi_7O_9I_3$, suggesting that there existed more efficient interfacial charge separation and transfer due to the construction of internal electric field with a direction from n-type

Bi_5O_7I to n-type $Bi_7O_9I_3$ after the formation of $Bi_7O_9I_3/Bi_5O_7I$ heterojunction structure. The EIS was further investigated to detect the charge transfer efficiency of the $Bi_7O_9I_3$ and $Bi_7O_9I_3$-450. It was well known that the semi-arc shape reflected the speed of electron transmission [27]. The large radius represented strong resistance to transport of electrons and holes. It was obviously observed that the $Bi_7O_9I_3$-450 could receive less resistance from the transfer of the charge from the Fig. 9 (b), which was in good agreement with the trend of photo-current density.

3.3. Photocatalytic mechanism for $Bi_7O_9I_3$-450 sample

The photocatalytic reaction responsible for the TCS degradation under simulated solar light irradiation might involve some reactive species, such as holes, hydroxyl ($\cdot$OH), electron (e^-), super oxidative ($\cdot O_2^-$) and singlet oxygen [24]. To further investigate the photocatalytic mechanism, the KI (5 mmol/L) [36], isopropanol (10 mmol/L) [42], $K_2Cr_2O_7$ (1 mmol/L) [43], benzoquinone (BQ 1 mmol/L) [44] and 2, 2, 6, 6-Tetramethylpiperidine (TEMP 0.1 mol/L) [45] were used as scavengers for h^+, $\cdot$OH, e^-, $\cdot O_2^-$, and singlet oxygen, respectively. As illustrated in Fig. 10 (a, b), the photo-degradation of TCS was significantly suppressed when the BQ and $K_2Cr_2O_7$ were added to the reaction system. It was noteworthy that the corresponding degradation rate constants were about 42 times and 13 times lower than the system with no scavengers, which suggested that $\cdot O_2^-$ and e^- played a pivotal role in the photocatalytic reaction system of $Bi_7O_9I_3$-450. The degradation rate constant had some influence with the addition of scavengers KI and TEMP, implying that h^+ and singlet oxygen were also active species responsible for photocatalytic degradation of TCS [41]. However, it was interesting that the photocatalytic efficiency was increased slightly when the isopropanol as $\cdot$OH scavengers was added to the reaction system. It was well known that the $\cdot$OH could be generated by direct hole oxidation or photo-generated electron induced multistep reduction of O_2 [46]. For $Bi_7O_9I_3/Bi_5O_7I$, the top valence band of $Bi_7O_9I_3$ (1.57 V vs. NHE, see below) and Bi_5O_7I (1.84 V vs. NHE, see below) were lower than that of $\cdot$OH/OH- (1.99 V vs. NHE) and $\cdot$OH/ H_2O (2.27 V vs. NHE), implying that the formation of $\cdot$OH didn't result from direct hole oxidation but the electron induced multistep reduction of O_2 [see Eq. (2–4)].

$$e^- + O_2 \rightarrow \cdot O_2^- \tag{2}$$

$$2\cdot O_2^- + 2H^+ \rightarrow O_2 + H_2O_2 \tag{3}$$

$$H_2O_2 + \cdot O_2^- \rightarrow \cdot OH + OH^- + O_2 \tag{4}$$

It could be seen from the above equations that the chemical reaction rate of Eq. (4) was sped up and then fasten reaction rates in the Eqs. (2) and (3) when $\cdot$OH was captured. These processes accelerated the

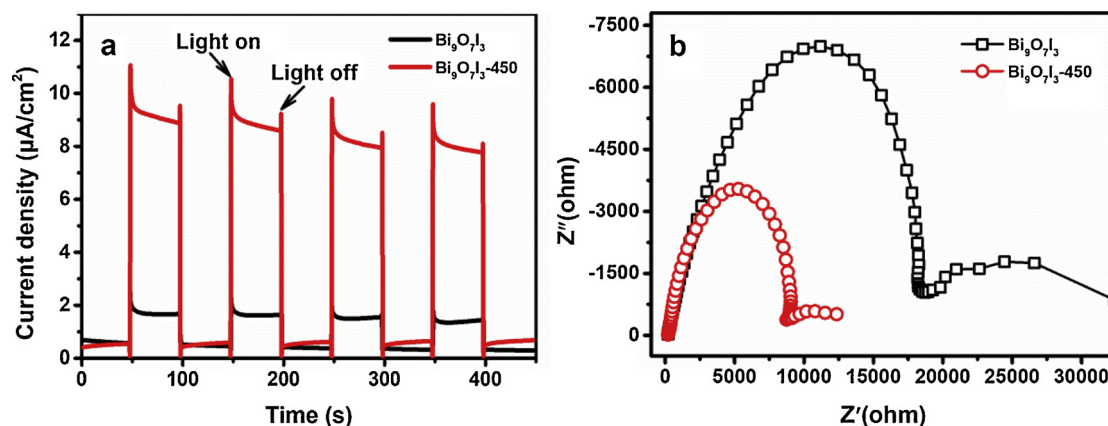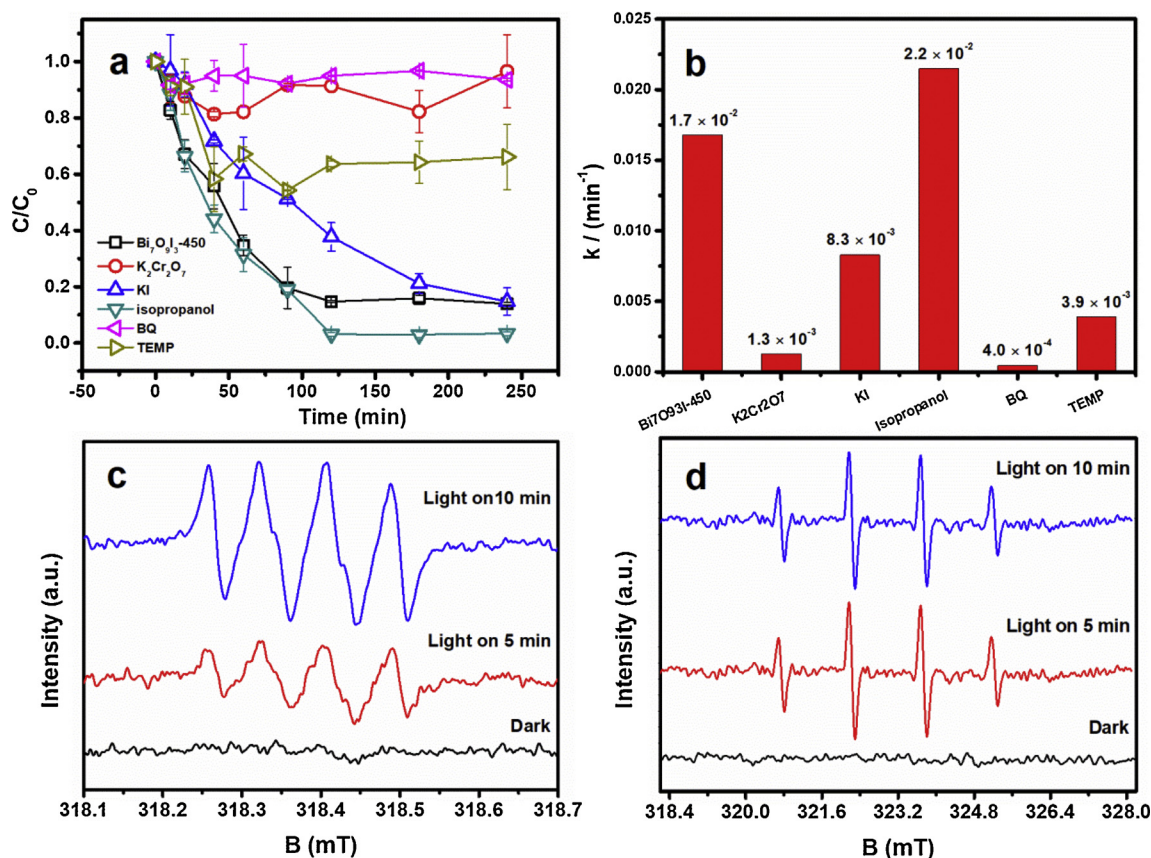**Fig. 9.** (a) Photo-current density of samples $Bi_7O_9I_3$ and $Bi_7O_9I_3$-450 with and without light illumination; (b) Nyquist plot of samples $Bi_7O_9I_3$ and $Bi_7O_9I_3$-450 recorded at applied potential of -0.5 V.

Fig. 10. Scavenger effects on degradation of TCS (a) and the reaction rate (b) of $Bi_7O_9I_3$-450 in the trapping experiments under simulated solar irradiation. ESR signals of the (c) DMPO-$\cdot O_2^-$ and (d) DMPO-$\cdot OH$ for the $Bi_7O_9I_3$-450 under simulated solar light irradiation.

electrons' depletion, regenerated more oxygen on the surface of catalyst, promoted the generation of $\cdot O_2^-$, and facilitated efficient separation of photo-generated carriers, and all of them modestly boosted the photocatalytic efficiency for TCS. Based on the above discussion, we hypothesized that $\cdot OH$ might play a slight role in TCS degradation. Electron spin resonance (ESR) spectroscopy with DMPO spin-trapping adducts was applied to further confirm the role of certain active species in the reaction system. As shown in Fig. 10 (c), no signal was detected in the dark. The four characteristic signals of $\cdot O_2^-$ radical species were observed when $Bi_7O_9I_3/Bi_5O_7I$ composite were exposed to the simulated solar irradiation, and the signal intensities of DMPO-$\cdot O_2^-$ increased with the irradiation time. The ESR results confirmed that $\cdot O_2^-$ could be generated in the presence of $Bi_7O_9I_3/Bi_5O_7I$ photocatalyst, which was in according with the trapping experiments of active species. In Fig. 10 (d), the characteristic signals of DMPO- $\cdot OH$ adducts could not be found in dark, but the four characteristic peaks with intensity ratio of 1:2:2:1 could be observed under simulated solar irradiation [47]. It was indicated that $\cdot OH$ could be generated in $Bi_7O_9I_3/Bi_5O_7I$ system for photocatalytic degradation of TCS.

Mott-Schottky (M–S) plots of samples $Bi_7O_9I_3$, $Bi_7O_9I_3$-450 and $Bi_7O_9I_3$-550 were measured. As shown in Fig. 11, the positive slope of the Mott-Schottky plot indicated that both $Bi_7O_9I_3$ and Bi_5O_7I were n-type semiconductors. The flat band potentials (E_f) of $Bi_7O_9I_3$, $Bi_7O_9I_3$-450 and $Bi_7O_9I_3$-550 were approximately -0.57, -0.91 and -0.94 V vs. Ag/AgCl, corresponding to -0.38, -0.71 and -0.74 V vs. NHE, respectively. Since the E_f of the n-type semiconductor might be considered approximately as the conduction band edge for estimating purposes [47–49], the conduction band potentials (E_{CB}s) of $Bi_7O_9I_3$ and Bi_5O_7I were assumed to be -0.38 and -0.74 V vs. NHE, respectively. The valence band potentials (E_{VB}s) of the two semiconductors could be estimated by the following equations:

$$E_{CB} = E_{VB} - E_g \qquad (5)$$

Where E_g is the band gap of semiconductor. The E_gs for $Bi_7O_9I_3$ and Bi_5O_7I are 1.95 and 2.58 V respectively in Fig. 11 (d), which are obtained by the following equation: $\alpha h\nu = A (h\nu - E_g)^{n/2}$, where α, h, ν, E_g, and A are the absorption coefficient, Planck constant, the light frequency, the band gap, and a constant, respectively. In this equation, n depends on the properties of the semiconductor. When the sample is direct semiconductor n = 1, and if n = 4 represents that the sample is indirect semiconductor. $Bi_7O_9I_3$ and Bi_5O_7I are indirect semiconductors [22,24]. Thus, the E_{VB}s of $Bi_7O_9I_3$ and Bi_5O_7I were calculated as 1.57 and 1.84 V vs. NHE respectively, which were closed to the results obtained from previous reports [50,51].

Based on the above results and discussion, the efficient separation and transfer of photo-generated carriers for the photocatalytic degradation of TCS was attributed to the in situ formation of n-n heterojunction at interfaces between n-$Bi_7O_9I_3$ and n-Bi_5O_7I, and illustrated in Scheme 2. Before the contact, the Fermi level of n-$Bi_7O_9I_3$ and n-Bi_5O_7I lied below their conduction band, and the Fermi level was the chemical potential of thermodynamic equilibrium. After forming of heterojunction, electrons were transferring from higher CB level to the lower one and the holes were moving simultaneously in opposite way until the Fermi level of both semiconductors reached a new equalization state, and finally forming an inside electric field between n-Bi_5O_7I and n-$Bi_7O_9I_3$. The photo-generated electrons transferred from the E_{CB} of the n-$Bi_7O_9I_3$ to the E_{CB} of n-Bi_5O_7I, meanwhile, the photo-generated holes transferred from the E_{VB} of n-Bi_5O_7I to the E_{VB} of the n-$Bi_7O_9I_3$ when $Bi_7O_9I_3/Bi_5O_7I$ composite was exposed to the simulated solar light irradiation. The transferred electrons could be trapped by the molecular oxygen to form $\cdot O_2^-$ radicals, and $\cdot O_2^-$ radicals further oxidized TCS absorbed on the surface of the photocatalysts. According to the trapping experiments, singlet oxygen also contributed to the TCS
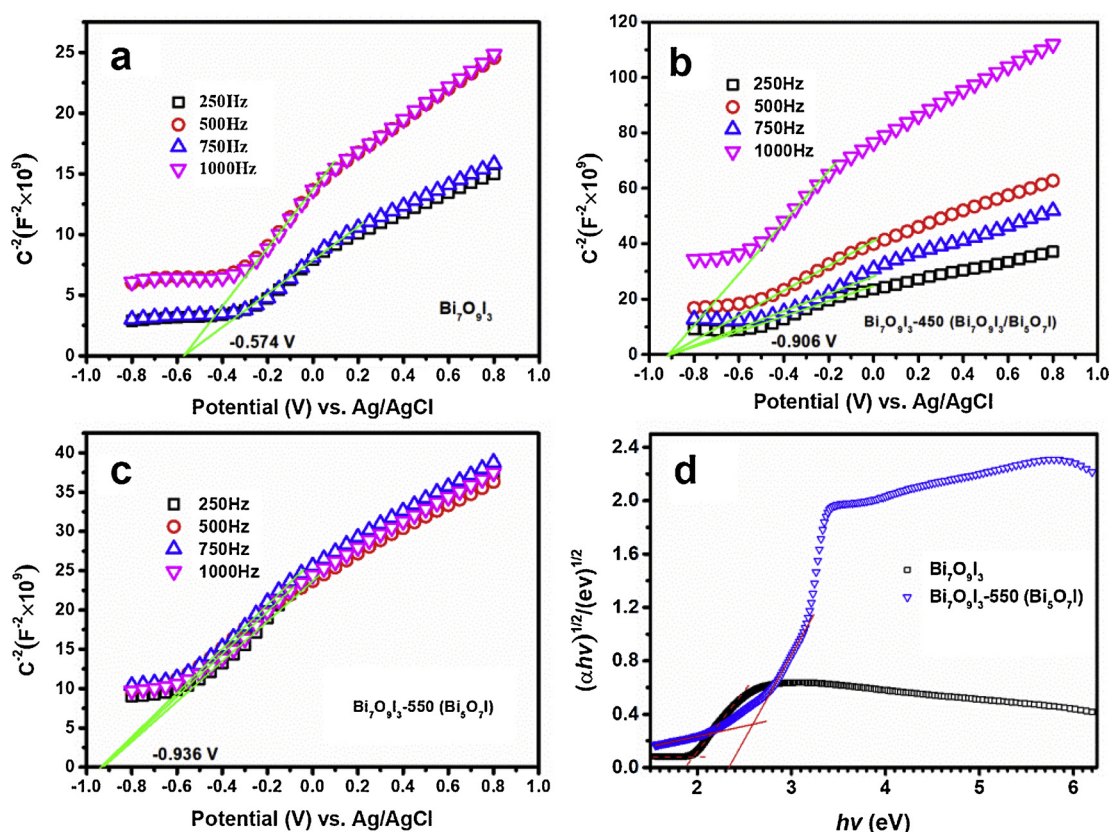
Fig. 11. Mott-Schottky plots of $Bi_7O_9I_3$ (a), $Bi_7O_9I_3$-450 (b), $Bi_7O_9I_3$-550 (c); the $(\alpha h\nu)^{1/2}$ *vs.* energy of absorbed light plots for band gap calculation of sample $Bi_7O_9I_3$ and $Bi_7O_9I_3$-550 (d).

degradation, which could be caused by the molecular oxygen absorbed the energy to produce $^1O_2$, and then $^1O_2$ further oxidized pollutants. Besides, the holes in the E_{VB} of n-$Bi_7O_9I_3$ migrated to the surface of the photocatalyst and oxidized pollutants. So the results showed that heterojunction n-$Bi_7O_9I_3$/n-Bi_5O_7I composites could efficiently promote the separation of the photo-generated electron-holes pairs. Finally, the photocatalytic efficiency for the degradation of TCS on n-$Bi_7O_9I_3$/n-Bi_5O_7I composites was enhanced under simulated solar light irradiation.
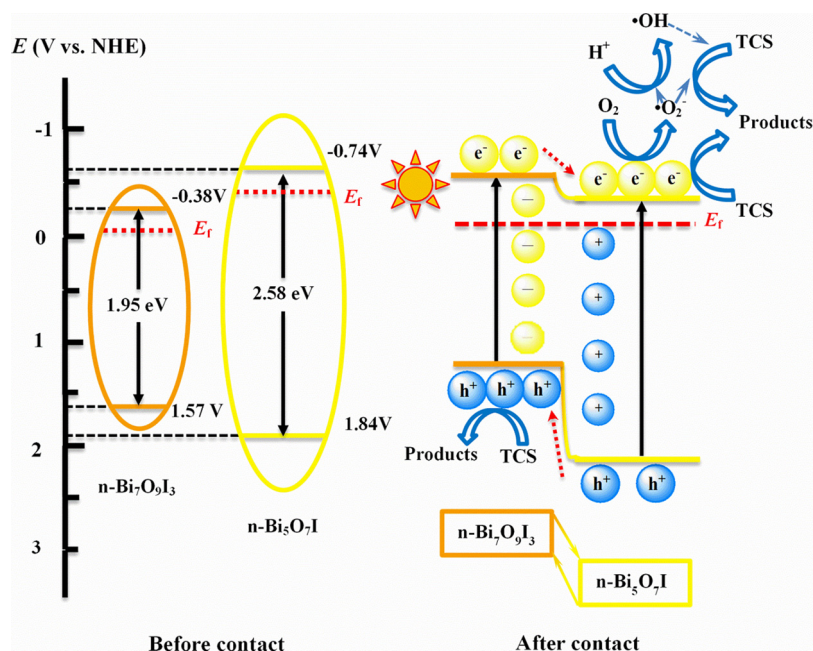
Scheme 2. Energy bands of n type $Bi_7O_9I_3$ and n type Bi_5O_7I, and the transfer of photo-generated carriers in the $Bi_7O_9I_3$/Bi_5O_7I heterojunction under simulated solar light irradiation.
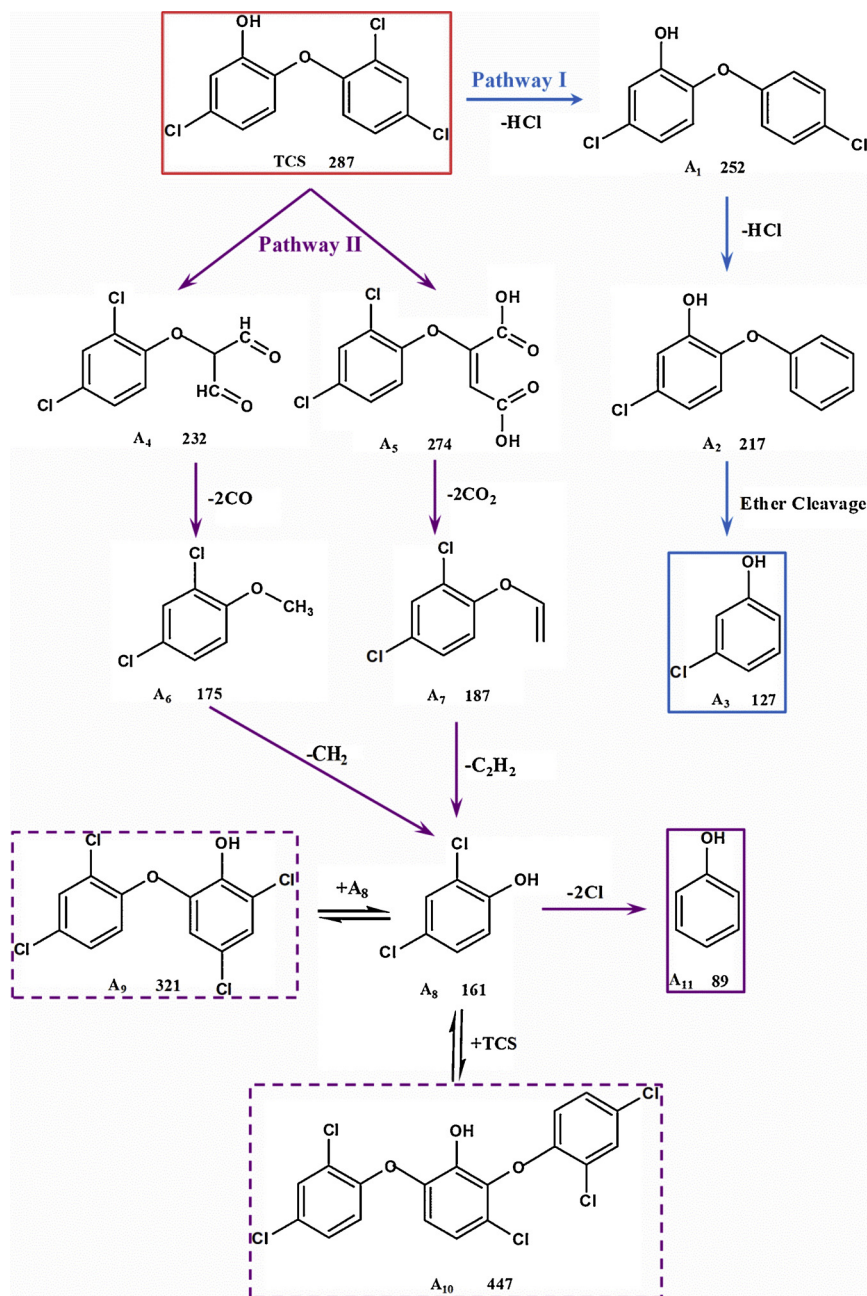
Fig. 12. Degradation products and reaction pathway of TCS.

3.4. Exploration of products and reaction pathways

The degradation products of TCS by $Bi_7O_9I_3$-450 were detected by high performance liquid chromatography-mass spectrometer (HPLC-MS), and the degradation reaction pathway was deduced on the basis of products and scavenger experiments. The eleven product ions at m/z 252, m/z 217, m/z 127, m/z 232, m/z 274, m/z 175, m/z 187, m/z 161, m/z 321, m/z 447 and m/z 89 were detected, and the temporal evolutions of the reaction products were shown in Fig. S3. According to radical scavenger experiments, the $\cdot O_2^-$ and e^- were the main active radicals in the degradation processes of TCS, and the singlet oxygen also contributed to the degradation of pollutants. Based on these results, two possible degradation pathways for TCS by $Bi_7O_9I_3$-450 could be speculated, and the result was presented in Fig. 12. The photocatalyst could produce a large amount of electrons under simulated solar light irradiation, and then the electrons could migrate to the surface of

catalyst. Firstly, TCS was attacked by electrons, contributing to the nucleophilic reactions on cation, so TCS was preliminary degraded by reductive dechlorination, and transformed into dichlorophenoxyphenol (A_1, m/z 252) which mainly resulted from the nucleophilic attack on carbocation by electrons [52]. The product monochlorophenoxyphenol (A_2, m/z 217) was obtained by the further dechlorination. The ion peaks with m/z 252 and 217 indicated the successive losses of Cl from the TCS (m/z 287). Secondly, the ether linkage of the A_2 was cleaved, and chlorophenol (A_3, m/z 127) was generated. The relative peak areas of the degradation products were presented in the Fig. S3, there could be clearly exhibited the trend of the product concentration. This degradation pathway was confirmed in the spectrum of TCS and the fragments of A_1 (m/z 252), which were shown in the Fig. S4 (a, b). The relative peak areas of dichlorophenoxyphenol (A_1) and monochlorophenoxyphenol (A_2) increased after 30 min of illumination and then decreased, which suggested that the products of A_1 and A_2 were
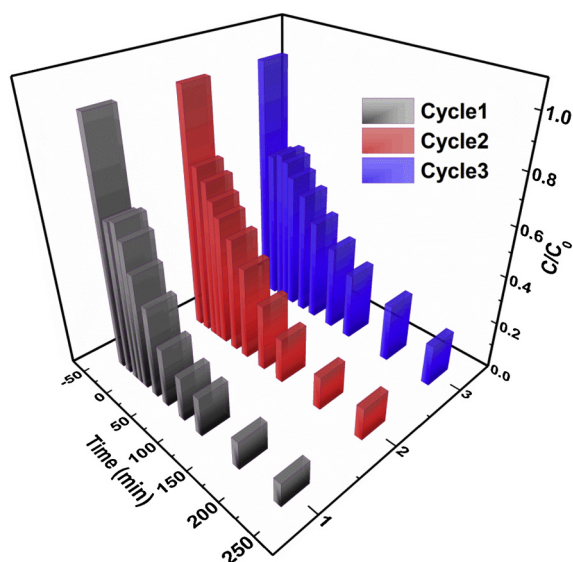
Fig. 13. Cycling runs for the photocatalytic performance of TCS in the presence of $Bi_7O_9I_3$-450 under simulated solar irradiation.

intermediates. However, the relative peak areas of chlorophenol (A_3) continued to increase until 240 min of irradiation, reflecting that A_3 was one of the final products.

Another pathway included two oxidation processes. The $\cdot O_2^-$ and singlet oxygen also contributed to the degradation of TCS, and played a major role in the oxidative reaction. Two ion peaks with m/z 274 and 232 were detected. It could be speculated that the hydroxylation reaction could take place in the less chlorinated benzene ring when TCS was subjected to $\cdot O_2^-$ species and singlet oxygen [53]. In these processes, some ring-opening products were generated, including 2-(2, 4-dichlorophenoxy) malonaldehyde (A_4, m/z 232) and 2-(2, 4-dichlorophenoxy) maleic acid (A_5, m/z 274). Subsequently, the products 2, 4-dichloroanisole (A_6, m/z 175) and 2, 4-dichlorostyrene ether (A_7, m/z 187) were generated by the loss of 2CO and $2CO_2$ from products A_4 and A_5. As shown in Fig. S4 (c, d), the fragment ion peaks with 175 and 187 resulted from the losses of CO and CO_2 from parent ions of 232 and 274, respectively. Furthermore, the loss of CH_2 and C_2H_2 from A_6 and A_7 resulted in the formation product of 2, 4-dichlorophenol (A_8, m/z 161). At the same time, 2, 4-dichlorophenol (A_8) could couple with another 2, 4-dichlorophenol or residual TCS, further transforming into the 2-(2, 4-dichlorophenoxy)-4, 6-dichlorophenol (A_9, m/z 321) and 2, 6-bis (2, 4-dichlorophenoxy)-3-chlorophenol (A_{10}, m/z 447), respectively. Finally, loss of 2Cl from the A_8 generated an ion peak at m/z 89 (A_{11}), which was identified phenol. According to Fig. S3, the amount of 2-(2, 4-dichlorophenoxy)-4, 6-dichlorophenol (A_9) fluctuated up and down, it was speculated that 2, 4-dichlorophenol (A_8) coupled with another 2, 4-dichlorophenol was in a reversible equilibrium state. The amount of the 2, 6-bis (2, 4-dichlorophenoxy)-3-chlorophenol (A_{10}) initially increased until 120 min of the light, and then the concentration dropped. It was mainly because of the increase of 2, 4-dichlorophenol (A_8) and the degradation of TCS in the reaction system, respectively. The fragmentation pathways of A_9 and A_{10} were displayed in Fig. S4 (e, f), which was consistent with the above analysis results. In brief, the reaction pathways for TCS mainly included two processes of reduction and oxidation, which involved dechloridation, the cleavage of the ether bond and the benzene ring-opening (in the less chlorinated benzene ring).

3.5. Stability of $Bi_7O_9I_3$-450 photocatalyst

To evaluate the optical stability of photocatalyst, recycling experiments of $Bi_7O_9I_3$-450 for the TCS degradation were implemented under simulated solar irradiation, and the result was shown in Fig. 13. The $Bi_7O_9I_3$-450 did not exhibit significant loss of photocatalytic performance after three recycling runs, and the photocatalytic degradation rate decreased to 77.80% from the pristine degradation efficiency of 89.28%. The slight decrease in degradation efficiency over three runs could be ascribed to the mass loss of catalyst during the washing procedure. The result indicated that the sample of $Bi_7O_9I_3$-450 exhibited a relatively stable photocatalytic performance without distinct photocorrosion during the degradation of TCS.

4. Conclusions

In summary, the $Bi_7O_9I_3/Bi_5O_7I$ n-n heterojunction photocatalyst was prepared through a facile and low cost method. The heterojunction structure of n-type $Bi_7O_9I_3$ and n-type Bi_5O_7I promoted the photogenerated carriers separation, and hence the photocatalytic performance of $Bi_7O_9I_3$ was enhanced for the degradation of TCS under simulated solar light irradiation. It was investigated that the electron, $\cdot O_2^-$ species, and singlet oxygen played critical part in the TCS degradation through trap experiments. The eleven products were identified by the HPLC-MS, including the organic acids and aldehydes, ether compound, phenoxyphenol, chlorophenol, and phenol. Two major reaction pathways, which involved dechlorination, the cleavage of the ether bond and the benzene ring-opening (in the less chlorinated benzene ring), were deduced. These were also helpful to better understand the mechanism of photo-degradation of TCS. This work might give us a new hint for better use of semiconductor heterojunctions to degrade emerging pollutants in the environment.

Appendix A. Supplementary data

Supplementary material related to this article can be found, in the online version, at doi:https://doi.org/10.1016/j.apcatb.2019.05.030.

References

[1] J. Liu, J. Wang, C. Zhao, J. Liu, H. Xie, S. Wang, J. Zhang, Z. Hu, Appl. Microbiol. Biotechnol. 101 (2017) 1653–1660.
[2] N. Stamatis, M. Antonopoulou, D. Hela, I. Konstantinou, J. Chem. Technol. Biotechnol. 89 (2014) 1145–1154.
[3] J. Liu, J. Wang, C. Zhao, A.G. Hay, H. Xie, J. Zhan, Appl. Microbiol. Biotechnol. 100 (2016) 1459–1467.
[4] S. Wang, J. Wang, Chem. Eng. J. 356 (2019) 350–358.
[5] J.C. Duran-Alvarez, B. Prado, D. Gonzalez, Y. Sanchez, B. Jimenez-Cisneros, Sci. Total Environ. 538 (2015) 350–362.
[6] J. Kim, H. Oh, B. Ryu, U. Kim, J.M. Lee, C.-R. Jung, Cy. Kim, J.-H. Park, Environ. Pollut. 236 (2018) 304–312.
[7] A.L. Heffernan, C. Baduel, L.M.L. Toms, A.M. Calafat, X. Ye, P. Hobson, S. Broomhall, J.F. Mueller, Environ. Int. 85 (2015) 77–83.
[8] R. Dou, J. Zhang, Y. Chen, S. Feng, Environ. Sci. Pollut. Res. 24 (2017) 8778–8789.
[9] Y. Chen, X. Lei, R. Dou, Y. Chen, Y. Hu, Z. Zhang, Environ. Sci. Pollut. Res. 24 (2017) 18640–18650.
[10] D. Wu, X. Wang, H. Wang, F. Wang, D. Wang, Z. Gao, X. Wang, F. Xu, K. Jiang, J. Colloid Interface Sci. 533 (2019) 539–547.
[11] T. Kanagaraj, S. Thiripuranthagan, Appl. Catal. B 207 (2017) 218–232.
[12] Y. Zhang, C. Lin, Q. Lin, Y. Jin, Y. Wang, Z. Zhang, H. Lin, J. Long, X. Wang, Appl. Catal. B 235 (2018) 238–245.
[13] Y. Chen, G. Zhu, M. Hojamberdiev, J. Gao, R. Zhu, C. Wang, X. Wei, P. Liu, J. Hazard. Mater. 344 (2018) 42–54.
[14] S.G. Fard, M. Haghighi, M. Shabani, Appl. Catal. B 248 (2019) 320–331.
[15] C. Liang, C.-G. Niu, L. Zhang, X.-J. Wen, S.-F. Yang, H. Guo, G.-M. Zeng, J. Hazard. Mater. 361 (2019) 245–258.
[16] M. Ji, Y. Liu, J. Di, R. Chen, Z. Chen, J. Xia, H. Li, Appl. Catal. B 237 (2018)

1033–1043.

[17] Y. Ao, K. Wang, P. Wang, C. Wang, J. Hou, Dalton Trans. 45 (2016) 7986–7997.

[18] L. Yosefi, M. Haghighi, Appl. Catal. B 220 (2018) 367–378.

[19] S. Bai, K. Tian, H. Fu, Y. Feng, R. Luo, D. Li, A. Chen, C.C. Liu, Sens. Actuators B Chem. 268 (2018) 136–143.

[20] C.S. Yaw, Q. Ruan, J. Tang, A.K. Soh, M.N. Chong, Chem. Eng. J. 364 (2019) 177–185.

[21] M. Sun, Q. Wei, Y. Shao, B. Du, T. Yan, L. Yan, D. Li, Appl. Catal. B 233 (2018) 250–259.

[22] C. Liu, H. Huang, X. Du, T. Zhang, N. Tian, Y. Guo, Y. Zhang, J. Phys. Chem. C 119 (2015) 17156–17165.

[23] W. Ai, J. Jiang, J. Zhu, Z. Fan, Y. Wang, H. Zhang, W. Huang, T. Yu, Adv. Eng. Mater. 5 (2015).

[24] C. Chang, L. Zhu, Y. Fu, X. Chu, Chem. Eng. J. 233 (2013) 305–314.

[25] X. Xiao, R. Hao, X. Zuo, J. Nan, L. Li, W. Zhang, Chem. Eng. J. 209 (2012) 293–300.

[26] R. He, J. Zhou, H. Fu, S. Zhang, C. Jiang, Appl. Surf. Sci. 430 (2018) 273–282.

[27] C. Chang, H.-C. Yang, N. Gao, S.-Y. Lu, J. Alloys. Compd. 738 (2018) 138–144.

[28] I. Tateishi, H. Katsumata, T. Suzuki, S. Kaneco, Catal. Lett. 147 (2017) 1503–1509.

[29] G. Wu, Y. Zhao, Y. Li, F. Zhang, J. Zhao, CrystEngComm 19 (2017) 2113–2125.

[30] Y. Bai, L. Ye, T. Chen, L. Wang, X. Shi, X. Zhang, D. Chen, ACS Appl. Mater. Interfaces 8 (2016) 27661–27668.

[31] H. Wang, Y. Liang, L. Liu, J. Hu, P. Wu, W. Cui, Appl. Catal. B 208 (2017) 22–34.

[32] C. Chang, L. Zhu, S. Wang, X. Chu, L. Yue, ACS Appl. Mater. Interfaces 6 (2014) 5083–5093.

[33] L. Hu, H. He, D. Xia, Y. Huang, J. Xu, H. Li, C. He, W. Yang, D. Shu, P.K. Wong, ACS Appl. Mater. Interfaces (2018).

[34] X. Zhou, C. Shao, S. Yang, X. Li, X. Guo, X. Wang, X. Li, Y. Liu, ACS Sustain. Chem. Eng. 6 (2018) 2316–2323.

[35] Y. Huang, H. Hu, S. Wang, M.-S. Balogun, H. Ji, Y. Tong, Appl. Catal. B 218 (2017) 700–708.

[36] S.-R. Zhu, Q. Qi, Y. Fang, W.-N. Zhao, M.-K. Wu, L. Han, Cryst. Growth Des. 18 (2018) 883–891.

[37] F.-Q. Ma, J.-W. Yao, Y.-F. Zhang, Y. Wei, RSC Adv. 7 (2017) 36288–36296.

[38] B. Long, Y. Huang, H. Li, F. Zhao, Z. Rui, Z. Liu, Y. Tong, H. Ji, Ind. Eng. Chem. Res. 54 (2015) 12788–12794.

[39] X. Xiao, Y. Lin, B. Pan, W. Fan, Y. Huang, Inorg. Chem. Commun. 93 (2018) 65–68.

[40] D. Yuan, L. Huang, Y. Li, Y. Xu, H. Xu, S. Huang, J. Yan, M. He, H. Li, RSC Adv. 6 (2016) 41204–41213.

[41] Y. Ao, K. Wang, P. Wang, C. Wang, J. Hou, Appl. Catal. B 194 (2016) 157–168.

[42] X.-J. Wen, C.-G. Niu, L. Zhang, G.-M. Zeng, Dalton Trans. 46 (2017) 4982–4993.

[43] Z. Yang, D. Dai, Y. Yao, L. Chen, Q. Liu, L. Luo, Chem. Eng. J. 322 (2017) 546–555.

[44] M.J. Islam, H.K. Kim, D.A. Reddy, Y. Kim, R. Ma, H. Baek, J. Kim, T.K. Kim, Dalton Trans. 46 (2017) 6013–6023.

[45] Y. Zhi, Z. Li, X. Feng, H. Xia, Y. Zhang, Z. Shi, Y. Mu, X. Liu, J. Mater. Chem. A 5 (2017) 22933–22938.

[46] C. Chang, Y. Fu, M. Hu, C. Wang, G. Shan, L. Zhu, Appl. Catal. B 142-143 (2013) 553–560.

[47] Y. Jia, S. Li, J. Gao, G. Zhu, F. Zhang, X. Shi, Y. Huang, C. Liu, Appl. Catal. B 240 (2019) 241–252.

[48] G. Zhu, M. Hojamberdiev, S. Zhang, S.T.U. Din, W. Yang, Appl. Surf. Sci. 467-468 (2019) 968–978.

[49] L. Zhang, Y. Hu, J. Zheng, J. Mater. Chem. A 5 (2017) 18664–18673.

[50] A. Chachvalvutikul, J. Jakmunee, S. Thongtem, S. Kittiwachana, S. Kaowphong, Appl. Surf. Sci. 475 (2019) 175–184.

[51] Y. Peng, Y.G. Mao, T. Liu, CrystEngComm 20 (2018) 4771–4780.

[52] J. Niu, Y. Dai, L. Yin, J. Shang, J.C. Crittenden, Phys. Chem. Chem. Phys. 17 (2015) 17421–17428.

[53] J. Chen, R. Qu, X. Pan, Z. Wang, Water Res. 103 (2016) 215–223.